Morphology of Polymers Precipitated from a Supercritical Solvent

Ashish K. Lele and Annette D. Shine
Dept. of Chemical Engineering, University of Delaware, Newark, DE 19716

The precipitation of polymers via the rapid expansion of a supercritical chlorodifluoromethane solution to ambient conditions across a fine diameter capillary has been studied experimentally. The morphology of the polymers precipitated—polycaprolactone, poly(methyl methacrylate) and a styrene/methyl methacrylate block copolymer—is influenced strongly by conditions of the expansion process. Conditions of high temperature, high polymer concentration, low pressure or low capillary L/D ratio enhance the formation of high aspect ratio fibers, while opposite conditions favor the formation of spherical particles of micron size. Each of the conditions favoring fiber formation favors precipitation farther upstream in the expansion process. Based on one-dimensional compressible flow calculations using a virial equation of state for pure solvent, it is proposed that fiber formation occurs when a polymer-rich phase is rejected from solution in the entry region to the capillary. The location of precipitation is shown to be crucial in determining the characteristic time scale for the density reduction process, which may be as small as 10^{-7} s.

Introduction

The rapid expansion of supercritical fluid solutions (RESS) is a relatively new process in which an organic or inorganic solute is precipitated into the sold state upon expansion of a dilute solution in a supercritical or near-critical solvent (Matson et al., 1987a). The expansion step in RESS occurs through a throttling device, such as a valve (Chang and Randolph, 1989), capillary (Petersen et al.,1986), or orifice (Mohamed et al., 1989), which supports a large pressure drop. During expansion, the solvent density decreases considerably, causing solute to be rejected from the solution due to low solubility at gas-like solvent density. The RESS process has been used to produce a variety of precipitate morphologies, such as thin films, fine diameter fibers, or narrow size distribution particles. The product morphology, however, can vary considerably depending on the choice of solution components and operating conditions used in the process (Matson et al., 1986a,b, 1987b; Petersen et al., 1987; Brand and Miller, 1988). RESS has potential commercial application for producing thin-film coatings (Sievers and Hansen, 1990), ceramic nanoparticles (Matson and Smith, 1989), and drug delivery microspheres (Tom and Debenedetti, 1991), so it is desirable to develop an understanding of the relationship between the RESS process and the morphology of the product.

However, an understanding of RESS process effects on morphology is still in its infancy. Thin films are believed to result from suppressed condensation, as a "molecular spray" impinges on a substrate (Matson et al., 1987b) or by reaction at a surface (Sievers and Hansen, 1990). Uniform-sized spheres may result from homogeneous nucleation in the highly supersaturated expanding solution (Matson et al., 1987a; Debenedetti, 1990). For polymeric solutes, which are the focus of the present work, RESS operating conditions can dramatically influence the morphology of the precipitate. At fixed solute concentration and pre-expansion pressure, Smith and coworkers observed that fibers were produced when the pre-expansion temperature was near the polymer melting point, and spherical particles were produced otherwise (Petersen et al.,1987). They postulated that fibers result from the entrainment of molten polymer droplets in the high-velocity gas stream.

Recently, Debenedetti (1990) examined theoretically the production of uniform particles from the RESS process by considering homogeneous nucleation in a highly supersaturated solution. In his treatment, however, the thermodynamic path along which changes in state variables occur during expansion

Correspondence concerning this article should be addressed to A. D. Shine.

Table 1. Polymers Precipitated from Chlorodifluoromethane

Polymer	MW^*	T_g(°C)	T_m**(°C)
Poly(methyl methacrylate)	50,000	126**	—
Isotactic poly(methyl methacrylate)	310,000	38*	156†
Polycaprolactone	14,000	−60*	60
Polystyrene/poly(methyl methacrylate) block copolymer	15,000 (S) 15,000 (M)	104**(S) 126**(M)	— —
Polyethylene succinate	11,000	−1*	108
Poly(hydroxybutyrate valerate)	670,000		155

*Reported by supplier.
**Measured in our laboratories.
†After annealing at 90°C for 72 h.

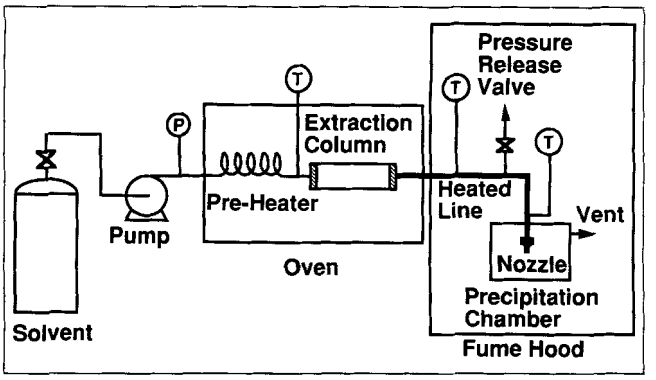

Figure 1. Experimental equipment.

was idealized (for example, isentropic, isenthalpic or isothermal) rather than specified by formulating the compressible flow problem. An understanding of the fluid dynamics of the expansion process is essential to a full description of RESS, because the changes in state variables, especially density, experienced by a fluid element during the expansion cause precipitation of the solute. RESS dynamics are also necessary to define the characteristic time for the process, which has been estimated at 10^{-5} s based on residence time in the capillary (Mohamed et al., 1989; Smith et al., 1986). Furthermore, the production of fibrous and elongated precipitate morphologies (Matson et al., 1987a) under some RESS conditions suggests that deformation resulting from the flow field might directly influence product morphology.

In this work, we present experimental observations of the morphology of polymers precipitated from chlorodifluoromethane solvent via RESS. Changes in pressure, capillary L/D ratio, and polymer dissolution temperature (concentration), in addition to the temperature effect already reported (Petersen et al., 1987; Matson et al., 1987a), cause a variation of the precipitate morphology between fibers and spheres. To explain these observations, we model flow in the RESS apparatus as a one-dimensional adiabatic expansion using a real fluid equation of state for pure solvent and demonstrate that fibers are produced when the predicted fluid density at the entrance to the throttling capillary falls below that required for polymer solubility. In an apparatus such as the one we use experimentally, the characteristic time for precipitation may range over several orders of magnitude, depending on the solubility-density relationship for the solution. The most rapid characteristic times could be achieved in a potential commercial process at the expense of increased solvent recompression costs.

Experimental Methods

Materials

Two classes of polymer solutes were examined in this study: semicrystalline aliphatic polyesters, especially polycaprolactone (PCL), and methacrylate-containing polymers, especially amorphous poly(methyl methacrylate) (PMMA), and a styrene/methyl methacrylate block copolymer, (SMAC). Table 1 lists the polymers studied, along with the molecular weights, and glass transition (T_g) and melting (T_m) temperatures. The PMMA and the SMAC were supplied by the Procter & Gamble Company. Each of these polymers was synthesized by anionic polymerization and had a polydispersity index of less than 1.1. This PMMA has a higher content of syndiotacticity, and therefore a higher T_g (126°C) than conventional PMMA prepared by free radical polymerization (108°C). Secondary standard polycaprolactone was purchased from Scientific Polymer Products and had $\overline{M}_w$ of 14,600 and $\overline{M}_n$ of 9,300. Polyethylene succinate and isotactic poly(methyl methacrylate) were purchased from Scientific Polymer Products, and poly(hydroxybutyrate valerate) was purchased from Aldrich; these were used without further purification.

As none of the polymers was found to be soluble in carbon dioxide, the solvent used in all our experiments was chlorodifluoromethane (CDFM, DuPont Freon 22), which has a critical temperature of 96°C and a critical pressure of 49.34 atm (Altunin, 1987). The hydrogen atom in this hydrochlorofluorocarbon is capable of interacting with the ester linkage in the polymer chains, causing solubilization of the polymers (Meilchen et al., 1991).

Equipment

The experimental RESS apparatus is shown in Figure 1. The system is similar to that used by Mohamed et al. (1989). CDFM solvent is filtered and then pressurized by a minipump set at the flow rate required to produce the desired pressure. It passes through a preheater and an extraction column that are enclosed in an oven for temperature control. The preheater consists of coiled stainless-steel tubing, while the extraction column is a stainless-steel pipe. For each experimental run, the column is charged with about 0.1 g of polymer. A glass wool plug is packed at the outlet to prevent any physical entrainment. As the solvent passes through the column, the polymer is dissolved in it. Because of the low mass-transfer coefficients for dissolving high-molecular-weight polymers and the fairly high flow rates needed to maintain pressure in our RESS apparatus, the solvent was not saturated with polymer after passing through the extraction column, and concentration could not be precisely controlled independent of the system pressure. A rough means of varying polymer concentration was established by adjusting the temperature of the oven containing the extraction column. Because the polymers studied had greater solubility in CDFM at lower temperatures, the rate of mass transfer to the stream (and hence polymer concentration) could be enhanced by lowering the oven temperature.

After the dissolution step, the solution is heated if necessary and maintained at the desired pre-expansion temperature as it passes through a length of tubing (2.77 mm id) wrapped with

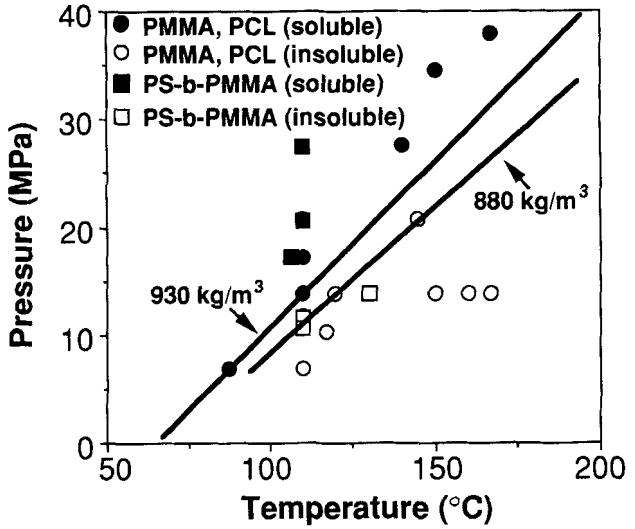

Figure 2. Detectable solubility of polymers in chlorodifluoromethane.

heating tapes. Pre-expansion conditions are always set such that precipitation is avoided inside the tubing, as evidenced by the absence of polymer deposition in the tubing. Precipitation of the polymer occurs when the solution is throttled across a fine-diameter orifice, either 30 or 50 μm in diameter, which was laser-drilled in a stainless-steel plate 0.254 mm thick. Thus, the L/D ratio of the orifice used in these studies is either 8.47 or 5.08. The orifice plate sits in a stainless-steel cap threaded onto the heated tubing. The orifice is examined under a microscope before and after each experiment to ensure that it is not clogged with minute particles. Operating pressure is measured by a pressure gauge before the preheater, while three thermocouples measure the temperatures in the oven (dissolution temperature) in the heated line and at a point just before the orifice (pre-expansion temperature), as shown in Figure 1. Precipitation to ambient conditions is performed inside a metal enclosure located in a fume hood; the precipitate is collected on a suitable substrate such as a microscope slide, and the gaseous solvent can be condensed to be recycled.

The mass-flow rate of pure solvent across the expansion orifice was also measured as a function of upstream pressure. In these experiments, the extraction column was removed, and a wet test meter was used downstream of the orifice to measure the volumetric flow rate of the expanded solvent.

Characterization

Characterization of the precipitate morphology was done by optical microscopy with a Nikon Optiphot-2 microscope by scanning electron microscopy (Phillips 501) for size measurement and by differential scanning calorimetry (DuPont DSC9900) at a heating rate of 20°C/min. Molecular weights were determined by gel permeation chromatography (Hewlett Packard HP 1090) using polystyrene standards.

Experimental Results

Polymer solubility

Because of mass-transfer limitations on polymer dissolution in our RESS apparatus, quantitative solubilities of polymers in CDFM could not be determined from flow experiments in this equipment. However, as a screening technique, we were able to establish whether a polymer exhibited appreciable solubility in CDFM by noting whether or not detectable (milligram) quantities of polymer precipitate could be recovered from the expansion. The solubility was further substantiated by qualitatively examining the polymer, if any, remaining in the extraction column after an experimental run. Molecular weights of the precipitated polymers were the same as those of the starting material, as determined by GPC. Figure 2 shows the range of detectable solubility of PCL, PMMA and SMAC as a function of dissolution temperature and pressure. For these polymers, solubility is enhanced at conditions of higher solvent density: increased pressure or decreased temperature. The lines in the figures represent predictions of constant density from the virial equation of state of Altunin (1987). For a solvent density of 930 kg/m^3 or higher, the polymers were found soluble in CDFM, while none of the polymers in Table 1 was found to be soluble at a CDFM density below 880 kg/m^3. (At its normal boiling point, the density of liquid CDFM is 1,410 kg/m^3). The conditions required for minimum detectable solubility are remarkably similar for the polymers studied, probably because of the similarity of the polymer solubility parameters. However, the amount of polymer collected under identical conditions varied among the polymers in the order PCL > PMMA > SMAC.

Morphology of precipitated polymers

Figure 3 shows optical photomicrographs of polycaprolactone precipitate obtained from an initial pressure of 13.8 MPa. The precipitate in Figure 3a, obtained from a 90°C pre-expansion temperature and a 50-μm orifice, occurs as approximately spherical particles 1 to 5 μm in diameter, which occasionally agglomerate into larger aggregates. The precipitate in Figure 3b, obtained from a 110°C pre-expansion temperature and a 50 μm orifice, occurs predominantly as 2- to 7-μm-diameter fibers, although particles were always found to accompany the fibers. If the precipitate density is assumed to be that of the starting material, then the observed fiber diameters are at least a factor of 5 larger than those that would result from continuous extrusion of the solution. These fibers extinguish light between crossed polarizers when the polarizer or analyzer has its optical axis parallel to the fiber axis. This demonstrates that the PCL crystallites in the fibers are highly oriented, probably due to a high extension rate in the RESS apparatus. For a pre-expansion temperature of 145°C and a 50-μm orifice, the recovered precipitate (Figure 3c) has a spherulitic morphology typical of melt-crystallized polycaprolactone, because at this elevated temperature, cooling due to solution expansion is insufficient to lower the post-expansion temperature below the polymer melting point (60°C). The precipitate shown in Figure 3d was obtained from a 110°C pre-expansion temperature and a 30-μm orifice. It shows a morphology that might be described as elongated particles and apparently represents a state intermediate between fibers and powder. Except for the morphologies in Figures 3c and 3d, all other polymers examined showed morphologies similar to the fibers and powders in Figures 3a and 3b.

Table 2 summarizes the morphologies of PMMA, SMAC and PCL precipitated from CDFM under conditions where

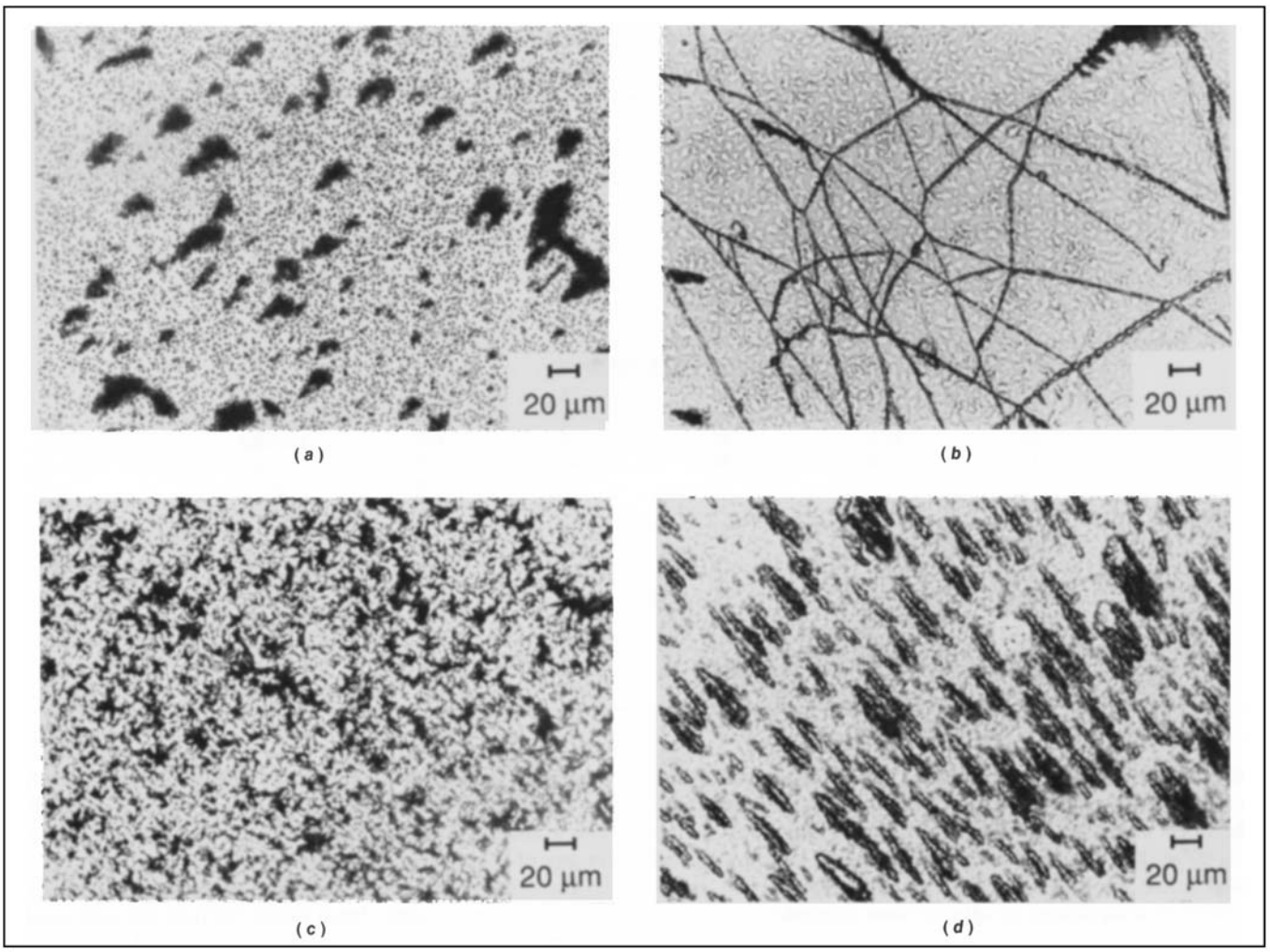

Figure 3. Optical photomicrographs of polycaprolactone precipitated from CDFM at 13.8 MPa.

(a) 90°C initial temperature, 50-μm capillary;
(b) 110°C initial temperature, 50-μm capillary;
(c) 145°C initial temperature, 50 μm-capillary;
(d) 110°C initial temperature, 30-μm capillary.

four variables were adjusted: upstream pressure, pre-expansion temperature, dissolution temperature (inversely related to polymer concentration), and the diameter of the capillary. The effect of changes in each of these variables on the precipitate morphology is the same qualitatively for all the polymers studied.

As observed by Petersen et al. (1987), we note that an increase in pre-expansion temperature, under certain experimental conditions, can lead to a transition from powder morphology to fibrous morphology (for example, SMAC at 17.2 MPa; 110°C vs. 130°C). The occurrence of fibers, however, is clearly unrelated to any solid polymer "melting" phenomenon, as Petersen et al. postulated, because fibers of PMMA were produced at pre-expansion temperatures as low as 110°C, even though amorphous PMMA has no melting point, and the T_g of the neat PMMA used in these experiments was 126°C. Besides an increase in temperature, a decrease in pressure also results in the powder-to-fiber morphology transition, as can be seen from the series of pressure runs conducted for each polymer. This combination of pressure and temperature effects suggest that solutions with lower density are more likely to produce fibers from the RESS process. Solution concentration also affects precipitate morphology. For identical pressure (10.7 MPa) and pre-expansion temperature (110°C), PMMA expanded across a 50-μm orifice produces fibers at a dissolution temperature of 70°C, but powder at a dissolution temperature of 100°C.

In addition to the thermodynamic variables of pressure, temperature and concentration, a process design variable, namely the diameter of the expansion capillary (or L/D ratio, since L was fixed), was also found to influence the morphology of the polymer precipitate. For example, PMMA precipitated across a 50-μm orifice at 10.7 MPa and a pre-expansion temperature of 110°C produces a powder precipitate, while fibers are produced under the same conditions with a 30-μm orifice. This dependence of product morphology on apparatus geometry indicates that the fluid mechanics of the process is important, at least insofar as the gross (fiber vs. powder) mor-

Table 2. Morphology of RESS-Precipitated Polymers

Case No.	Pres. MPa	Orifice μm	T_{oven} °C	$T_{pre\text{-}exp}$ °C	Morphology
Poly(methyl methacrylate)					
1	8.27	30	100	110	Fiber
2	11.0	30	100	110	Fiber
3	13.8	30	100	110	Fiber
4	17.2	30	100	110	Powder
5	20.7	30	100	110	Powder
6	17.2	30	70	130	Fiber
7	10.7	50	70	110	Fiber
8	10.7	50	100	110	Powder
9	10.7	50	100	130	Fiber
Polystyrene/poly(methyl methacrylate) block copolymer					
10	13.8	30	75	110	Fiber
11	20.7	30	75	110	Powder
12	27.6	30	75	110	Powder
13	17.2	30	100	110	Powder
14	17.2	30	100	130	Fiber
15	10.7	50	75	110	Fiber
Polycaprolactone					
16	13.8	30	100	110	Elongated
17	17.2	30	100	110	Powder
18	20.7	30	100	110	Powder
19	13.8	50	90	90	Powder
20	13.8	50	100	110	Fiber
21	13.8	50	100	145	Spherulitic

phology of the product is concerned. This importance is further underscored by the observation of a high axial orientation in the fibers produced. Hence, in the following sections, we develop the fluid dynamics of the expansion of the supercritical fluid across the orifice and interpret the experimental observations of morphology in light of these dynamics.

Compressible Flow Dynamics of RESS

Figure 4 shows a schematic of the RESS process. A dilute solution at some initial pressure and temperature (P_0, T_0) expands adiabatically across a capillary nozzle and into a supersonic free jet issuing from the capillary end. Frictional interaction with background gases eventually causes deceleration of the jet in a compression shock front. It is important to note that fluid expansion takes place throughout the RESS process. First, acceleration of the subsonic flow in the entrance region to the capillary causes a drop in solvent density. Next, frictional losses (Fanno flow) inside the capillary nozzle further expand the fluid so that sonic conditions are reached at the capillary exit and the flow is choked. Finally, the fluid is expanded further in the supersonic flow occurring in the free jet region upstream of the shock. Depending on the solubility characteristics of the solution, solute segregation may occur in any of these expansion regions.

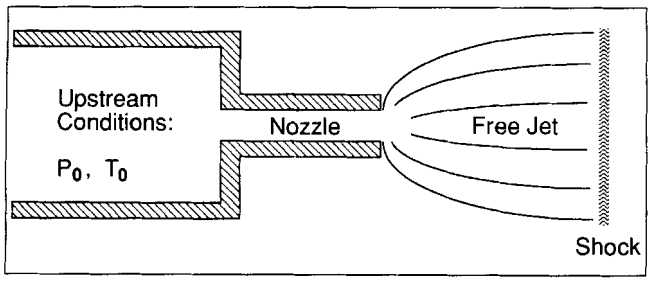

Figure 4. RESS process.

The initial conditions in the RESS process are such that the fluid exists in a highly dense phase, so that the well-studied dynamics of the adiabatic expansion of an ideal gas (Lapple, 1943; Murphy and Miller, 1984) are not directly applicable to RESS. Here, we present real fluid calculations for the flow of chlorodifluoromethane, the solvent used in our experimental work, into and through a capillary. Except for the equation of state (EOS), the assumptions used here are the same as those for the ideal gas case. Entry region and capillary flow are treated as adiabatic, one-dimensional, axially varying, steady-state flows. The assumption of a one-dimensional flow precludes monitoring local conditions upstream in the large diameter tube or reservoir, but nevertheless allows calculation of overall drops in pressure, temperature, and density due to the entry region. Capillary flow is modeled as adiabatic, but not isentropic since friction causes an entropy increase.

The set of governing equations in the capillary is as follows:

Continuity:

$$u\frac{d\rho}{dx}+\rho\frac{du}{dx}=0 \tag{1}$$

Momentum:

$$\rho u\frac{du}{dx}+\frac{dP}{dx}=-\frac{2fu^2\rho}{D} \tag{2}$$

Energy:

$$\rho u\frac{dh}{dx}-u\frac{dP}{dx}=\frac{2fu^3\rho}{D} \tag{3}$$

where x is the axial coordinate, u is the axial velocity, ρ is density, P is pressure, D is the capillary diameter, f is the Fanning friction factor, and h is the specific enthalpy. When these equations are combined with the EOS, the axial variation in pressure, temperature, density, and velocity can be solved for in terms of the conditions at the capillary entrance. The state variables at the entrance of the capillary are obtained by assuming an isentropic, adiabatic flow from the reservoir to the entrance.

Because the polymer solutions used experimentally were extremely dilute (<300 ppm), all calculations were performed using an EOS for pure solvent. The EOS of Altunin (1987) was used; it expresses the compressibility factor, z, as a virial expansion in ρ and T, in the temperature range of 285 to 473 K and the pressure range of 0.3 to 35 MPa. For this EOS:

$$P = z\rho RT \tag{4}$$

where R is the universal gas constant, and the compressibility factor is given by:

$$z = 1 + \sum_{i=1}^{8} \sum_{j=0}^{4} b_{ij} \frac{\rho^i}{\tau^j} \tag{5}$$

Here, τ is the reduced temperature, T/T_c, and the b_{ij}'s are constants given in the original reference.

Since the equation of state expresses the compressibility factor in terms of density and temperature, it is convenient to express the axial variation of all other dependent variables (P, h, u, and so on) likewise in terms of density and temperature. Equations 6-8 were derived by combining Eqs. 1-4 using a procedure analogous to that outlined by Thorley and Tiley (1987). Appendix A summarizes this derivation.

Density variation:

$$\frac{d\rho}{dx} = -\frac{2f\rho}{D}\left(\frac{M^2}{1-M^2}\right)\left[1 + \frac{R}{C_v}\left\{z + T\left(\frac{\partial z}{\partial T}\right)_\rho\right\}\right] \tag{6}$$

Temperature variation:

$$\frac{dT}{dx} = \frac{2fu^2}{C_v D} + \frac{RT}{\rho C_v}\left[z + T\left(\frac{\partial z}{\partial T}\right)_\rho\right]\frac{d\rho}{dx} \tag{7}$$

Velocity variation:

$$\frac{du}{dx} = -\frac{u}{\rho}\frac{d\rho}{dx} \tag{8}$$

where M is the local Mach number and C_v is the heat capacity at constant volume.

Equations 6-8, coupled with the equation of state Eq. 5, were solved by a simple forward marching finite difference scheme. The friction factor was assumed to be constant over the length of the capillary, with a numerical value equal to that for a perfectly smooth conduit. For the desired combination of pre-expansion pressure and temperature, a guess was made for the entrance temperature, which allowed estimations of the entrance density, pressure and Mach number from the isentropic assumption, the equation of state, and the continuity equation. These entry conditions were used as initial conditions for solving Eqs. 6-8. The capillary length was divided into 100 equal divisions, and a set of exit conditions was calculated for the chosen pre-expansion conditions and capillary length. The guess for the entrance temperature was checked by comparing the calculated exit conditions with those of choked flow. If the initial guess did not yield a calculated exit Mach number of unity (within 0.7%), a new entry temperature was assumed and the above procedure was repeated in its entirety.

During expansion, a real solvent may enter its two-phase region if P, T, and ρ drop below the critical values. In this case, we adopt the homogeneous equilibrium flow model (Starkman et al., 1964; Grolmes and Leung, 1984): we assume that when the solvent expands into the two-phase region, thermodynamic and mechanical equilibrium exists between the phases at all times. For these calculations, reliable saturation line information, that is, the vapor pressure, liquid density and gas density as a function of the fluid temperature, is required. The vapor pressure and liquid density functions were given by Altunin (1987), while we approximated the gas density, ρ_g, along the saturation line by an analogous equation:

$$\frac{\rho_g}{\rho_c} = 1 + \sum_{j=1}^{4} c_j (1-\tau)^{j/3} \tag{9}$$

The c_j's were obtained by curve-fitting Altunin's experimental data with a nonlinear regression subroutine (IMSL, ZXSSQ), and are shown in Appendix B.

Inside the two-phase region of the solvent, the equation of state (Eq. 5) does not predict the thermodynamic properties accurately. Hence, when the solvent enters this region during expansion, Eqs. 6-8 cannot be used. In this case, we adopt a procedure suggested by Leung and Grolmes (1987); it is outlined briefly here.

The integrated forms of Eqs. 1-3 can be written as:

$$G = u\rho \tag{10}$$

$$h_0 = h(T,\rho) + \frac{G^2}{2\rho^2} \tag{11}$$

$$dx = -\frac{D}{2f}\left(\frac{\rho dP}{G^2} - \frac{d\rho}{\rho}\right) \tag{12}$$

where G is the mass flux. Any condition of local choking should satisfy:

$$G = \rho\sqrt{\frac{dP}{d\rho}} \tag{13}$$

Substituting Eq. 13 into Eq. 12 shows that for local choking $dx = 0$. The calculation of conditions at the entrance to the capillary is the same as mentioned before. Equation 11 is then solved to give the fraction of the liquid phase formed during expansion.

As a check on the validity of the above procedure, the results of the calculations were used to predict the choked mass flux and the thermodynamic state of the solvent. Figure 5 shows a plot of measured and predicted choked mass flux vs. pre-

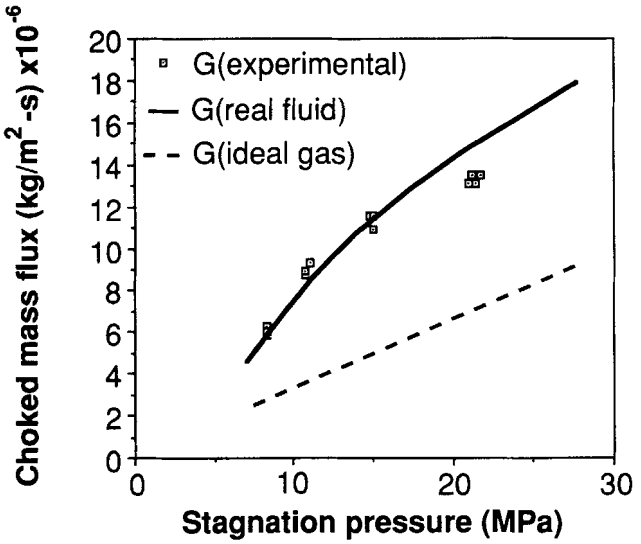

Figure 5. Choked mass flux of chlorodifluoromethane vs. initial pressure.

Pre-expansion temperature = 110°C; orifice ID = 30 μm; L/D = 8.47.

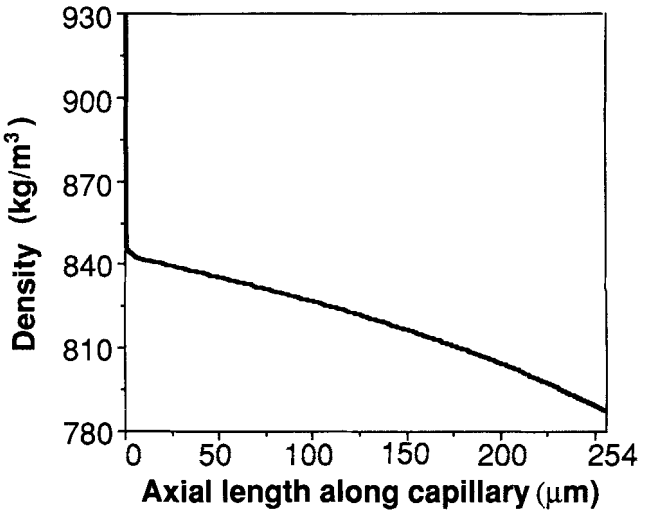

Figure 7. Predicted density variation for choked flow of chlorodifluoromethane in a capillary.

Upstream conditions are 13.8 MPa, 110°C. Orifice has ID = 30 μm, L/D = 8.47.

expansion (stagnation) pressure for a stagnation temperature of 110°C; Figure 6 shows a similar plot for $T_0 = 195$°C. A 30-μm orifice with an aspect ratio of 8.47 was used in both experiments and calculations. For a given solvent flow rate (as maintained by the liquid minipump), the application of a mechanical vacuum across the orifice did not lower the upstream pressure. This demonstrated that as expected, due to the high ratio of upstream to ambient (expansion) pressure, the flow was choked and the solvent flow rate was the maximum possible for the given upstream temperature and pressure. For the dilute polymer solutions used in the precipitation experiments,the measured CDFM flow rate was the same as for the case of pure solvent flow under the same conditions.

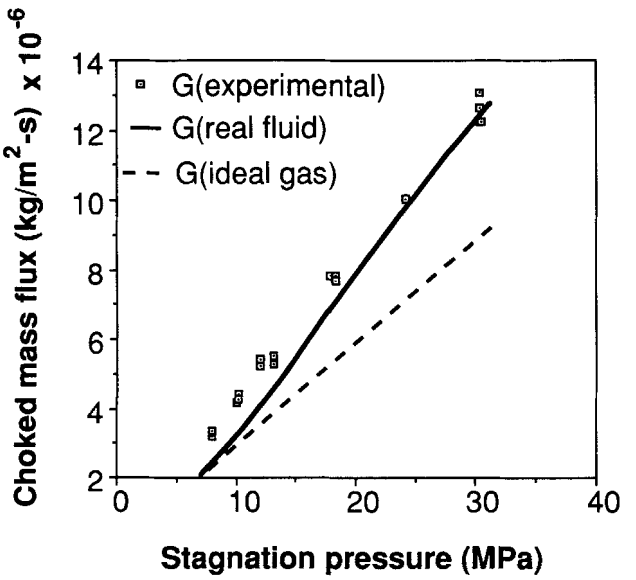

Figure 6. Choked mass flux of chlorodifluoromethane vs. initial pressure.

Pre-expansion temperature = 195°C; orifice ID = 30 μm; L/D = 8.47.

The real fluid equation of state predictions are seen to fit the experimental mass-flow rate data reasonably well. In particular, the real fluid calculations provide a much better fit to the experimental data than do ideal gas calculations, especially at the lower temperature. All real gas conditions in Figure 5 passed through the solvent liquid-vapor envelope, while none of those in Figure 6 did, with solvent remaining in the supercritical state up to the capillary exit.

Perhaps the most important assumption in these calculations is that of homogeneous equilibrium flow. This model frequently underpredicts the mass flux (Hesson and Peck, 1958; Starkman et al., 1964) of a flashing liquid or a saturated vapor for a given set of stagnation conditions. Our calculations, however, do not underpredict the experimental data, suggesting that the homogeneous equilibrium flow model is valid.

Equations 1-5 were solved by the procedure described above and used to calculate the local state variables and velocity in a 30-μm capillary. Figure 7 shows the variation of density along the axial length of the capillary for stagnation conditions of 13.8 MPa and 110°C. A zone of large density reduction is seen in the entry region. Table 3 presents values of state variables at the entrance and exit of the capillary for capillaries of different aspect ratios. The frictional contribution to the total

Table 3. Effect of Capillary Aspect Ratio on Chlorodifluoromethane Expansion*

State Variable	L/D = 0	L/D = 8.47	L/D = 167
Entrance P (MPa)		6.54	11.9
Entrance T (°C)		95.9	107.1
Entrance ρ (kg/m³)		846	913
Exit P (MPa)	4.31	4.41	4.59
Exit T (°C)	88.7	89.6	91.8
Exit ρ (kg/m³)	801	788	750

*Pre-expansion conditions: 13.8 MPa, 110°C, 929 kg/m³

change in density (stagnation density minus exit density) is less for a small aspect ratio orifice, but the entry region drop in density is significantly larger. As a result, the density ratios ρ_0/ρ_{entry} and ρ_{entry}/ρ_{exit} are functions of the capillary L/D; ρ_0/ρ_{entry} decreases with increasing L/D, while ρ_{entry}/ρ_{exit} increases with increasing L/D.

In the RESS process, a characteristic process time scale can be defined as the time required for a fluid element to experience a specified density decrease. The residence time in the capillary, as determined by integrating the substantial derivative of the density in Figure 7, is 1.9×10^{-6} s, during which time the density decreases by 7%. Because the flow continually accelerates along the centerline in all three flow regions (entrance, capillary, and free jet), the residence time is typical of density reduction inside the capillary, but not in the entrance or free jet regions. Because of the supersonic flow in the free jet, the rate of density reduction there is more rapid. For example, using the ideal gas calculations of Murphy and Miller (1984) we estimate that density decreases in the free jet region by over an order of magnitude in 4×10^{-7} s. An analogous time scale cannot be determined exactly for entry region flow, due to the one-dimensional flow assumption, but the characteristic time scale for density reduction in this region would be considerably larger than that for capillary flow, because in entry flow the characteristic velocity is lower, while the characteristic length scale (the reservoir diameter) is larger. For example, isentropic flow of an ideal gas through a converging conical nozzle with length equal to the reservoir diameter, which produces the same density drop as the abrupt contraction in Figure 7, has a residence time of 2×10^{-3} s. Thus, if solute precipitation occurs farther upstream in the RESS process, it will also occur at a slower rate. Since precipitation rate can have a profound influence on precipitate morphology, the location of phase separation in RESS may be important in determining product morphology.

The rapid (10^{-7} s) estimate for density decrease will represent the characteristic time for solute precipitation in RESS, if density reduction is the rate-limiting step for solute precipitation and if the initial solution density is high enough to suppress any phase separation in the entry region or inside the capillary. The former condition may not be met in all cases; for example, the time lag for homogeneous solute nucleation of phenanthrene from supercritical CO_2 at 318 K can range from 10^{-9} to 10^{-5} s, depending on conditions (Debenedetti,1990). Satisfying the latter condition may be prohibitively expensive in a large-scale process, since it would require that the solution initially be "overpressurized." For example, for an ideal nozzle with no frictional losses, delaying precipitation until the free jet region would require that the initial solution density, ρ_0, be about 60% higher than the minimum density required for solubility. Hence, recompression costs to recycle the expanded solvent would be proportionately increased.

At 0.1 MPa and 20°C, the density of CDFM is 3.60 kg/m^3, so Figure 7 clearly demonstrates (Matson et al.,1987a), that most of the density drop in RESS occurs in the free jet region of the expansion. This, however, does not imply that solute precipitation during RESS will occur in the free jet region. Rather, because of the large entry region drop in density for short capillaries in an actual RESS process, it is possible that precipitation of a solute from an expanding supercritical solution may occur in this entry region. For large L/D ratio capillaries, most of the drop in density occurs due to frictional flow in the capillary, so in this case, precipitation will likely occur there. In the following discussion of our experimental results on precipitation of polymer solutes from CDFM, we shall relate the location of precipitation to the morphology of the precipitate.

Table 4. State Predictions for Experimental Conditions

Case No.	Entry ρ kg/m^3	Entry State	Exit ρ kg/m^3	Exit State
Fibers				
9	595	Supercritical	511	Supercritical
1	709	Near-critical	670	Saturated Liquid
7	781	Near-critical	743	Saturated Liquid
15	781	Near-critical	743	Saturated Liquid
2	799	Liquid	750	Saturated Liquid
6	795	Supercritical	685	Supercritical
14	795	Supercritical	685	Supercritical
20	835	Liquid	791	Saturated Liquid
3	846	Liquid	788	Saturated Liquid
10	846	Liquid	788	Saturated Liquid
Elongated particles				
16	846	Liquid	788	Saturated Liquid
Powder				
8	781	Near-critical	743	Saturated Liquid
4	887	Liquid	820	Saturated Liquid
13	887	Liquid	820	Saturated Liquid
17	887	Liquid	820	Saturated Liquid
5	917	Liquid	844	Saturated Liquid
11	917	Liquid	844	Saturated Liquid
18	917	Liquid	844	Saturated Liquid
19	951	Liquid	928	Saturated Liquid
12	963	Liquid	880	Saturated Liquid

Discussion

The experimental conditions favoring the formation of fibers—low pre-expansion pressure, high pre-expansion temperature, high polymer concentration, and low capillary L/D ratio—all cause the solubility limit of the solution to be reached relatively early (upstream) in the RESS process. The rate of density reduction is lower in the upstream regions of RESS than in the downstream regions, so fibers are formed in a relatively slower process than are powders.

To determine the likely location of phase separation in RESS, we have performed numerical calculations for pure solvent expansion for each of the sets of conditions run experimentally; Table 4 summarizes these calculations. Fibers are clearly produced at conditions of lower entry (or exit) density, with powder production occurring at higher densities. The sole exception to this trend is case 8, which produced powder under conditions with relatively low density. We have no conclusive explanation for this reproducible discrepancy and suspect that a better understanding of the solubility behavior of the solutions could help to explain it, since case 8 differed from the fiber-producing case 7 only by solution concentration.

Since our experimental solubility determinations indicate negligible polymer concentrations in solutions with density below about 880 kg/m^3, we note that based on the predictions in Table 4, this solubility limit is reached for fiber-forming conditions before the solution enters the capillary, while the

limit is reached inside the capillary for powder-forming conditions. Under our experimental conditions, the solubility limit was predicted to be achieved beyond the capillary exit only in case 19 (where initial conditions were below the solvent critical point), because the necessary combination of pressure and flow rate was beyond the range of our minipump. Table 4 also suggests that the predicted state of the solvent (supercritical, near-critical, liquid, or two-phase) is apparently not significant in determining the morphology of the polymer precipitate. For the experimental conditions studied, the solvent was predicted to enter the two-phase region very near the exit of the capillary, which was downstream of the point where the solubility limit was reached.

An estimation of the time scale for powder precipitation can be made for case 12, which involved the highest pressure used experimentally. Since solubility experiments indicate measurable solubility above 930 kg/m^3 and negligible solubility below 880 kg/m^3, a reasonable estimate for the precipitation time scale would be the time required for a fluid element to traverse this solvent density range. In case 12, this entire density range occurs inside the capillary, where our calculations are applicable; we predict that density is lowered from 930 to 880 kg/m^3 in 6.1×10^{-7} s. Other experimental cases would have longer time scales, but we cannot estimate them from our 1-D flow model.

Low-molecular-weight solutes generally precipitate out of solution by a process of nucleation and growth, whereby the growing precipitate phase consists of pure solute. Polymers, especially amorphous polymers, undergo phase separation by a liquid-liquid process (Flory, 1953), whereby both the solution and precipitate phases contain both solvent and polymer. Even if the precipitate phase contains a relatively small amount of solvent, it may exhibit a dramatically depressed glass transition temperature. This plasticization effect has also been observed for SCF solvents (Wissinger and Paulaitis, 1987).

The occurrence of a highly oriented, fibrous precipitate under process conditions below the normal polymer T_g can be explained by fluid-fluid phase separation. The polymer-rich precipitate phase contains sufficient solvent so that it is plasticized and deformable under the local process conditions. The polymer becomes stretched in the axial direction due to the large extensional component of deformation in that direction, resulting from the fluid expansion. Equilibrium between polymers and CDFM under ambient conditions (at which CDFM exists as a gas) dictates that there be practically no solvent in the polymer phase as collected. Therefore, as the fluid expands further in RESS (beyond the point of initial phase separation), solvent is removed completely from the polymer-rich phase, leaving a dry precipitate. Differential scanning calorimetry data on precipitates support this, because no T_g depression is observed in the precipitate. The fluid-fluid phase separation hypothesis also suggests a plausible explanation for the occurrence of powder precipitate along with fiber precipitate. Powder may form downstream of the fiber formation point when polymer precipitates from the solvent-rich phase formed during the fluid-fluid-phase separation or may develop as a result of fiber breakup later in the RESS process.

Because the mechanism of polymer solution phase separation, either nucleation and growth (NG) or spinodal decomposition (SD), is known to influence morphology, a brief consideration of these mechanisms as the potential origin of the observed morphology differences in RESS-precipitated polymers is warranted. Typically, NG produces a spherical or globular precipitate, and SD a "lacy" structure (Caneba and Soong, 1987; Schaaf et al., 1987), so an analogy to our RESS powder and fiber morphologies could be drawn. However, a differentiation of phase separation mechanism based on precipitate morphology is still unequivocal (McMaster, 1975; Tsia and Torkelson, 1990). Hence, in the absence of thermodynamic or kinetic data, it is not possible to attribute the occurrence of the fiber morphology in our RESS precipitate to SD and spheres to NG. We believe this would be unlikely, however, since SD is more likely to occur with a deep, fast quench, and our data indicate that powder morphology is favored under such conditions.

Conclusions

Experimental investigations of the effect of process conditions on the morphology of polymers precipitated via the rapid expansion of a supercritical solution across an orifice show that increasing temperature, increasing polymer concentration, decreasing pressure, or decreasing L/D ratio of the capillary can cause a change in morphology from fine-diameter powder to high aspect ratio fibers. The temperature need not be above the normal melting point or glass transition temperature of the polymer in order for fibers to result. However, the high level of axial orientation in the fibers indicates that the polymer precipitated in a deformable state, probably as a polymer-rich fluid phase. Spherical particles usually accompanied the occurrence of fibers; these particles may have precipitated from the solvent-rich fluid phase or been caused by fiber breakup.

Expansion of the solution during RESS takes place in the entry region to the orifice, inside the capillary-like orifice and in the free jet region downstream of the orifice exit. The rate of density reduction increases as a fluid element progresses farther downstream. Experimental conditions favoring fiber formation also favor polymer precipitation farther upstream.

To identify the probable location of phase separation for fibers and powder, the adiabatic expansion of pure solvent from reservoir conditions to the exit of the capillary was analyzed. A real-gas, virial equation of state with density and temperature as the independent variables was used in the one-dimensional numerical flow calculations. The occurrence of fibers coincided with predictions that phase separation would occur during entry to the orifice, while powder morphology was found experimentally when calculations predicted that the solubility limit would be reached inside the orifice itself. Due to pressure limitations on the pump used, our experiments did not probe the operating regime where calculations indicated that solute phase separation would occur in the free jet region. The predicted occurrence of solvent flashing did not correlate with any morphological observations, because any solvent evaporation predicted to occur generally took place considerably downstream of the polymer precipitation point.

The characteristic time scale for RESS can be as short as 10^{-7} s, if solute precipitation can be delayed until beyond the entry region to the capillary exit. Such a short time scale may rival that for homogeneous nucleation and could likely produce precipitates with interesting, nonequilibrium properties. In practice, however, this would require a higher upstream solution density or a lower solute concentration than that re-

quired to achieve a saturated solution; either of these conditions would directly influence process economics through increased solvent compression costs.

Acknowledgment

This work was supported by the Procter & Gamble Company through its University Exploratory Research Program. We are grateful to Dr. Steven Smith of Proctor & Gamble for his suggestions and assistance.

Notation

b_{ij} = constants for CDFM equation of state (Eq. 5)
c_j = constants for CDFM saturated vapor density (Eq. 9)
C_V = real fluid heat capacity at constant volume
C_v^o = ideal gas heat capacity at constant volume
D = diameter of capillary
f = Fanning friction factor
G = mass flux
h = specific enthalpy
L = length of capillary
M = Mach number
P = pressure
P_0 = pre-expansion pressure
R = universal gas constant
T = temperature
T_c = critical temperature
T_g = glass transition temperature
T_m = melting temperature
T_0 = pre-expansion temperature
u = axial velocity
x = axial direction
z = compressibility factor

Greek letters

β_j = constants for CDFM heat capacity (Eq. A15)
ρ = density
ρ_c = critical density
ρ_g = saturated vapor density
ρ_0 = pre-expansion density
τ = reduced temperature, T/T_c

Literature Cited

Altunin, V. V., *Thermophysical Properties of Freons*, Vol. 2, T. B. Selover, Jr., translator, Hemisphere, Washington, DC (1987).
Brand, J. I., and D. R. Miller, "Ceramic Beams and Thin Film Growth," *Thin Solid Films*, **166**, 139 (1988).
Caneba, G. T., and D. S. Soong, "Polymer Membrane Formation Through the Thermal Inversion Process: 1. Experimental Study of Membrane Structure Formation," *Macromol.*, **18**, 2538 (1985).
Chang, C. J., and A. D. Randolph, "Precipitation of Microsize Organic Particles from Supercritical Fluids," *AIChE J.*, **35**(11), 1876 (1989).
Debenedetti, P. G., "Homogeneous Nucleation in Supercritical Fluids," *AIChE J.*, **36**(9), 1289 (1990).
Flory, P. J., *Principles of Polymer Chemistry*, p. 451, Cornell Univ. Press, Ithaca, NY (1953).
Grolmes, M. A., and J. C. Leung, "Scaling Considerations for Two Phase Critical Flows," *Multiphase Flow and Heat Transfer Part III, Part A: Fundamentals*, p. 549, T. N. Verziroglu and A. E. Bergles, eds., Elsevier, Amsterdam (1984).
Hesson, J. C., and R. E. Peck, "Flow of Two Phase CO_2 Through Orifices," *AIChE J.*, **4**(2), 207 (1958).
Lapple, C. E., "Isothermal and Adiabatic Flow of Compressible Fluids," *Trans. Amer. Inst. Chem. Eng.*, **39**, 385 (1943).
Leung, J. C., and Grolmes, M. A., "The Discharge of Two-Phase Flashing Flow in a Horizontal Duct," *AIChE J.*, **33**(3), 524 (1987).
Matson, D. W., J. L. Fulton, R. C. Petersen, and R. D. Smith, "Rapid Expansion of Supercritical Fluid Solutions: Solute Formation of Powders, Thin Films, and Fibers," *Ind. Eng. Chem. Res.*, **26**, 2298 (1987).
Matson, D. W., R. C. Petersen, and R. D. Smith, "Production of Powders and Films by the Rapid Expansion of Supercritical Solutions," *J. Mat. Sci.*, **22**, 1919 (1987).
Matson, D. W., R. C. Petersen, and R. D. Smith, "Formation of Silica Powders from the Rapid Expansion of Supercritical Solutions," *Adv. Ceram. Mat.*, **1**, 242 (1986).
Matson, D. W., R. C. Petersen, and R. D. Smith, "The Preparation of Polycarbosilane Powders and Fibers During the Rapid Expansion of Supercritical Fluid Solutions," *Mat. Lett.*, **4**, 429 (1986).
Matson, D. W., and R. D. Smith, "Supercritical Fluid Technologies for Ceramic-Processing Applications," *J. Am. Ceram. Soc.*, **72**, 871 (1989).
McMaster, L. P., "Aspects of Liquid-Liquid Phase Transition Phenomenon in Multicomponent System," *Copolymers, Polyblends and Composites*, Adv. in Chemistry Ser., No. 142, p. 43, A. J. Platzer, ed., Washington, DC (1975).
Meilchen, M. A., B. M. Hasch, and M. A. McHugh, "Effect of Copolymer Composition on the Phase Behavior of Mixtures of Poly(Ethylene-co-Methyl Acrylate) with Propane and Chlorodifluoromethane," *Macromol.*, **24**, 4874 (1991).
Mohamed, R. S., P. G. Debenedetti, and R. K. Prud'homme, "Effects of Process Conditions on Crystals Obtained from Supercritical Mixtures," *AIChE J.*, **35**, 325 (1989).
Murphy, H. R., and D. R. Miller, "Effects of Nozzle Geometry on Kinetics in Free-Jet Expansion," *J. Phys. Chem.*, **88**, 4474 (1984).
Petersen, R. C., D. W. Matson, and R. D. Smith, "Rapid Precipitation of Low Vapor Pressure Solids from Supercritical Fluid Solutions: The Formation of Thin Films and Powders," *J. Amer. Chem. Soc.*, **108**, 2100 (1986).
Petersen, R. C., D. W. Matson, and R. D. Smith, "The Formation of Polymer Fibers From the Rapid Expansion of Supercritical Fluid Solutions," *Polym. Eng. Sci.*, **27**, 1693 (1987).
Sandler, S. I., *Chemical and Engineering Thermodynamics*, p. 139, Wiley, New York (1989).
Schaaf, P., B. Lotz, and J. C. Wittmann, "Liquid-Liquid Phase Separation and Crystallization in Binary Polymer Systems," *Polymer*, **28**, 193 (1987).
Sievers, R. E., and B. N. Hansen, "Chemical Deposition Methods Using Supercritical Fluid Solutions," U.S. Patent No. 4,970,093 (1990).
Smith, R. D., J. L. Fulton, R. C. Petersen, A. J. Kopriva, and B. W. Wright, "Performance of Capillary Restrictors in Supercritical Fluid Chromatography," *Anal. Chem.*, **58**, 2057 (1986).
Starkman, E. S., V. E. Schrock, K. F. Neusen, and D. J. Maneely, "Expansion of Very Low Quality Two Phase Fluid Through a Convergent-Divergent Nozzle," *J. Basic Eng., Trans. ASME*, 247 (1964).
Tom, J. W., and P. G. Debenedetti, "Nucleation of Biocompatible Polymers," *Proc. Int. Symp. Supercritical Fluids*, p. 229 (1991).
Thorley, A. R. D., and C. H. Tiley, "Unsteady and Transient Flow of Compressible Fluids in Pipelines—a Review of Theoretical and Some Experimental Studies," *Int. J. Heat and Fluid Flow*, **8**, 3 (1987).
Tsia, F., and J. M. Torkelson, "Roles of Phase Separation Mechanism and Coarsening in the Formation of Poly(methyl methacrylate) Asymmetric Membranes," *Macromol.*, **23**, 775 (1990).
Wissinger, R. G., and M. E. Paulaitis, "Swelling and Sorption in Polymer-CO_2 Mixtures at Elevated Pressures," *J. Polym. Sci. B*, **25**, 2497 (1987).

Appendix A

The governing equations are:

$$u\frac{d\rho}{dx}+\rho\frac{du}{dx}=0 \tag{A1}$$

$$\rho u\frac{du}{dx}+\frac{dP}{dx}=-\frac{2fu^2\rho}{D} \tag{A2}$$

$$\rho u\frac{dh}{dx}-u\frac{dP}{dx}=\frac{2fu^3\rho}{D} \tag{A3}$$

$$P = z\rho RT \tag{A4}$$

Since the equation of state uses ρ and T as independent variables, $z = z(\rho, T)$, we need to express P and h in terms of ρ and T. Taking the logarithm of Eq. A4:

$$\ln P = \ln z + \ln \rho + \ln R + \ln T \tag{A5}$$

and differentiating with respect to x yields:

$$\frac{dP}{dx} = \frac{P}{z}\frac{dz}{dx} + \frac{P}{\rho}\frac{d\rho}{dx} + \frac{P}{T}\frac{dT}{dx} \tag{A6}$$

But, $z = z(\rho, T)$, therefore:

$$\frac{dz}{dx} = \left(\frac{\partial z}{\partial \rho}\right)_T \frac{d\rho}{dx} + \left(\frac{\partial z}{\partial T}\right)_\rho \frac{dT}{dx} \tag{A7}$$

Thus,

$$\frac{dP}{dx} = P\left[\frac{1}{\rho} + \frac{1}{z}\left(\frac{\partial z}{\partial \rho}\right)_T\right]\frac{d\rho}{dx} + P\left[\frac{1}{T} + \frac{1}{z}\left(\frac{\partial z}{\partial T}\right)_\rho\right]\frac{dT}{dx} \tag{A8}$$

With ρ and T as independent variables, the enthalpy can be expressed as (Sandler, 1989):

$$dh = C_v dT + d\left(\frac{P}{\rho}\right) + \frac{1}{\rho^2}\left[P - T\left(\frac{\partial P}{\partial T}\right)_\rho\right]d\rho \tag{A9}$$

Combining this with Eq. A4 gives:

$$\frac{dh}{dx} = \left[C_v + RT\left(\frac{\partial z}{\partial T}\right)_\rho + Rz\right]\frac{dT}{dx} + \left\{RT\left(\frac{\partial z}{\partial \rho}\right)_T - \frac{RT^2}{\rho}\left(\frac{\partial z}{\partial T}\right)_\rho\right\}\frac{d\rho}{dx} \tag{A10}$$

Substituting Eq. A8 into Eq. A2, and Eq. A9 into Eq. A3 with subsequent simplifications gives:

$$u\frac{d\rho}{dx} + \rho\frac{du}{dx} = 0 \tag{A11}$$

$$\rho u\frac{du}{dx} + \left[\frac{P}{\rho} + \frac{P}{z}\left(\frac{\partial z}{\partial \rho}\right)_T\right]\frac{d\rho}{dx} + \left[\frac{P}{T} + \frac{P}{z}\left(\frac{\partial z}{\partial T}\right)_\rho\right]\frac{dT}{dx} = -\frac{2fu^2\rho}{D} \tag{A12}$$

$$\rho C_v\frac{dT}{dx} - RT\left[T\left(\frac{\partial z}{\partial T}\right)_\rho + z\right]\frac{d\rho}{dx} = \frac{2fu^2\rho}{D} \tag{A13}$$

where C_v is calculated from the equation of state as:

$$C_v = T\left(\frac{\partial S}{\partial T}\right)_\rho = C_v^0 - R\sum_i\sum_j \frac{j(j-1)}{i} b_{ij}\frac{\rho^i}{\tau^j} \tag{A14}$$

Here C_v^0 is the ideal gas heat capacity given by the following equation:

$$C_v^0 = R\left(\sum_j \frac{\beta_j}{\tau^j} - 1\right) \tag{A15}$$

where b_{ij} and β_j are coefficients given by Altunin (1987).

Equations A11–A13 can be solved simultaneously for $(du)/(dx)$, $(d\rho)/(dx)$, and $(dT)/(dx)$ to yield Eqs. 6-8.

Appendix B

The coefficients in Eq. 9 obtained by a nonlinear regression analysis are:

$$c_1 = -1.40119257603628$$
$$c_2 = -2.458310578366022$$
$$c_3 = \ \ 4.724281519509824$$
$$c_4 = -1.752978974377223$$

Manuscript received Sept. 10, 1991, and revision received Mar. 19, 1992.